

# Constraints on the Heating of High Temperature Active Region Loops: Observations from *Hinode* and *SDO*

Harry P. Warren<sup>1</sup>, David H. Brooks<sup>2</sup>, and Amy R. Winebarger<sup>3</sup>

## ABSTRACT

We present observations of high temperature emission in the core of a solar active region using instruments on *Hinode* and *SDO*. These multi-instrument observations allow us to determine the distribution of plasma temperatures and follow the evolution of emission at different temperatures. We find that at the apex of the high temperature loops the emission measure distribution is strongly peaked near 4 MK and falls off sharply at both higher and lower temperatures. Perhaps most significantly, the emission measure at 0.5 MK is reduced by more than two orders of magnitude from the peak at 4 MK. We also find that the temporal evolution in broad-band soft X-ray images is relatively constant over about 6 hours of observing. Observations in the cooler *SDO*/AIA bandpasses generally do not show cooling loops in the core of the active region, consistent with the steady emission observed at high temperatures. These observations suggest that the high temperature loops observed in the core of an active region are close to equilibrium. We find that it is possible to reproduce the relative intensities of high temperature emission lines with a simple, high-frequency heating scenario where heating events occur on time scales much less than a cooling time. In contrast, low-frequency heating scenarios, which are commonly invoked to describe nanoflare models of coronal heating, do not reproduce the relative intensities of high temperature emission lines and predict low-temperature emission that is approximately an order of magnitude too large. We also present an initial look at images from the *SDO*/AIA 94 Å channel, which is sensitive to Fe XVIII.

*Subject headings:* Sun: corona

## 1. Introduction

Understanding the origin of high temperature plasma in the solar corona is one of the central problems in solar physics. The nanoflare concept represents one of the more popular theories for describing how energy stored in the Sun's magnetic field is converted into thermal energy (e.g., Parker

---

<sup>1</sup>Space Science Division, Naval Research Laboratory, Washington, DC 20375

<sup>2</sup>College of Science, George Mason University, 4400 University Drive, Fairfax, VA 22030

<sup>3</sup>NASA Marshall Space Flight Center, VP 62, Huntsville, AL 35812

1972, 1983). In nanoflare models turbulent photospheric motions drive the twisting and braiding of the magnetic field, which leads to the release of energy on small spatial scales as the accumulated topological complexity is dissipated by magnetic reconnection. Nanoflares are often modeled as impulsive heating events where the plasma is heated to very high temperatures ( $\sim 10$  MK) and then cools down through a combination of conduction, enthalpy flux, and radiation without being reheated. Furthermore, since these heating events are likely to occur on very small spatial scales an observed loop is assumed to be composed of many unresolved strands (e.g., Cargill 1994; Klimchuk & Cargill 2001; Patsourakos & Klimchuk 2006). This framework implies that nanoflare heated loops should have co-spatial hot and cool emission.

Observations at relatively cool coronal temperatures, however, have cast doubt on this heating scenario. Antiochos et al. (2003) and Nitta (2000), for example, have argued that cooling loops are often not observed in the core of an active region. This position has been supported by recent observations with the EUV Imaging Spectrograph (EIS) and the X-ray Telescope (XRT) on the *Hinode* mission (Kosugi et al. 2007). Warren et al. (2010) found no evidence for emission near 1 MK that was spatially correlated with emission at higher temperatures (3–5 MK) in the core of an active region. In this region the high temperature emission measured with XRT was observed to be relatively constant over many hours. Similarly, Brooks & Warren (2009) have found no evidence for strong variability in the intensities and Doppler shifts measured in the moss, the footpoints of the high temperature loops. These results suggest that high temperature loops are generally heated on very short time scales, much shorter than a characteristic cooling time, and do not cool down to lower temperatures.

Previous studies on the properties of high temperature emission in the core of an active region have failed to adequately address a fundamental question: what is the distribution of temperatures in the core of an active region? The EIS spectral range contains emission lines from Ca XIV–Ca XVII which provide excellent coverage of the critical 3–5 MK temperature range (see Del Zanna 2008; Warren et al. 2008). Observations of these lines in combination with other emission lines observed with EIS and observations with the thick XRT filters allow for the emission measure distribution to be computed over a very wide range of temperatures. The properties of the loop apexes along the line of sight are of particular importance. The dispersion in the temperature constrains the rate at which energy is input into high temperature loops and such information is critical for motivating physical models of this emission.

In this paper we present the analysis of new observations in the core of an active region taken after the launch of the *Solar Dynamics Observatory* (*SDO*). These observations feature spectroscopic observations from EIS and soft X-ray images from XRT on *Hinode*. These data show that the emission measure distribution for the loop apex is peaked at temperatures near 4 MK and falls off sharply at both higher and lower temperatures. At temperatures near 0.5 MK the emission measure is more than two orders of magnitude below the value at 4 MK. Simple hydrodynamic modeling suggests that these properties are inconsistent with low frequency nanoflare heating models. Such models predict low temperature emission that is approximately an order of

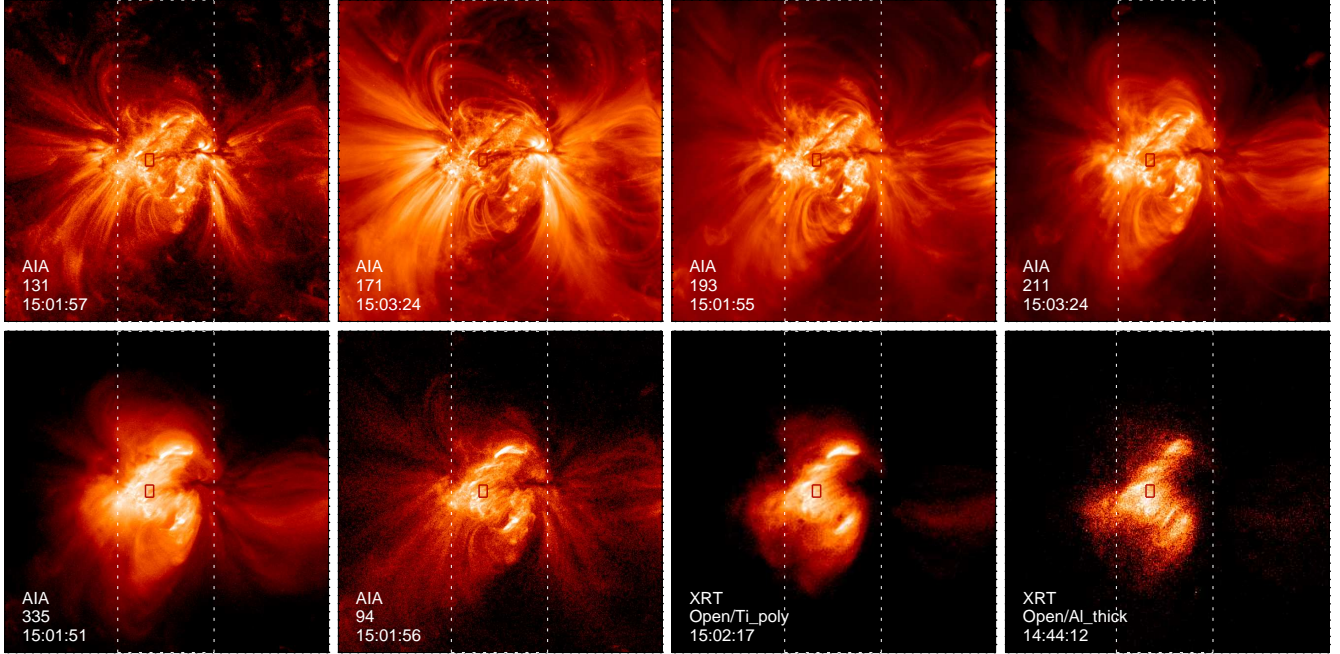


Fig. 1.— AIA and XRT observations of active region 11089 taken on 2010 July 23 near 15 UT. The field of view is  $384'' \times 384''$ , which is motivated by the size of the XRT images. The dotted line indicates the extent of the EIS raster. The small box indicates the region between the moss used to calculate the emission measure with EIS and XRT, and represents the physical conditions at the loop apexes along the line of sight. This region was chosen because it minimizes contamination from the moss. The electronic version of the manuscript includes movies of the AIA 171, 335, 94, and 131 Å channels.

magnitude larger than what is observed.

The high cadence ( $\sim 12$  s), high spatial resolution ( $0.6''$  pixels), narrow band images provided by the Atmospheric Imaging Assembly (AIA) on *SDO* provide additional information on the evolution of plasma at a wide range of temperatures. Images from channels dominated by 1 MK emission show only a few, isolated cooling loops in the moss regions, consistent with previous results. In this paper we also present some initial observations from the AIA 94 Å channel, which is sensitive to the Fe XVIII 93.94 Å line formed at about 7 MK. In small flares and microflares the expected progression from high temperature to low temperature emission is observed. In more quiescent areas of the active region core, however, the emission appears to be relatively constant, potentially consistent with what is observed in XRT.

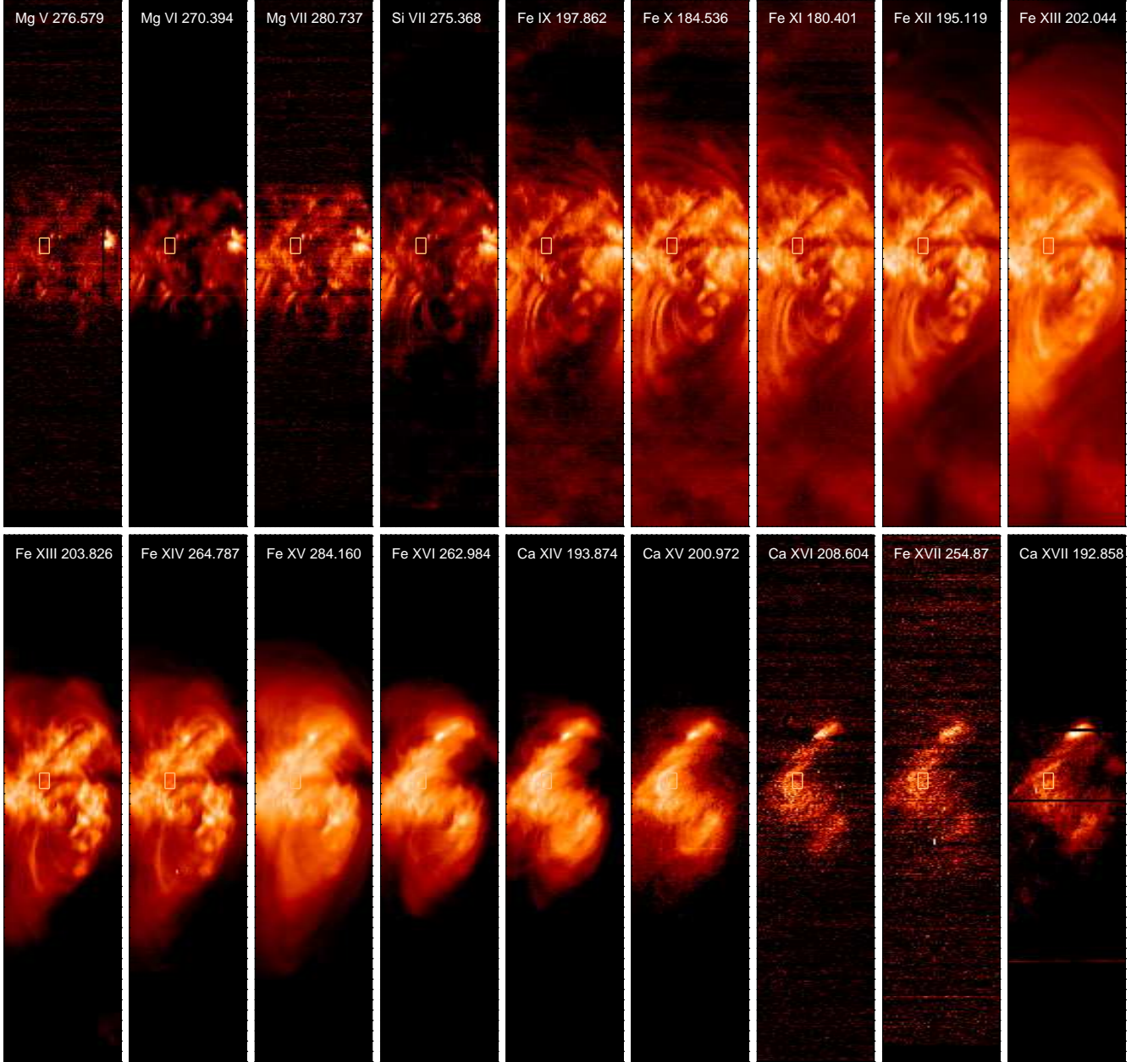


Fig. 2.— EIS observations of AR 11089 in various emission lines. The field of view is  $120'' \times 384''$ . The small box indicates the region between the moss used to calculate the active region “core” emission measure. The size of this region is  $10'' \times 15''$  or 75 spatial pixels.

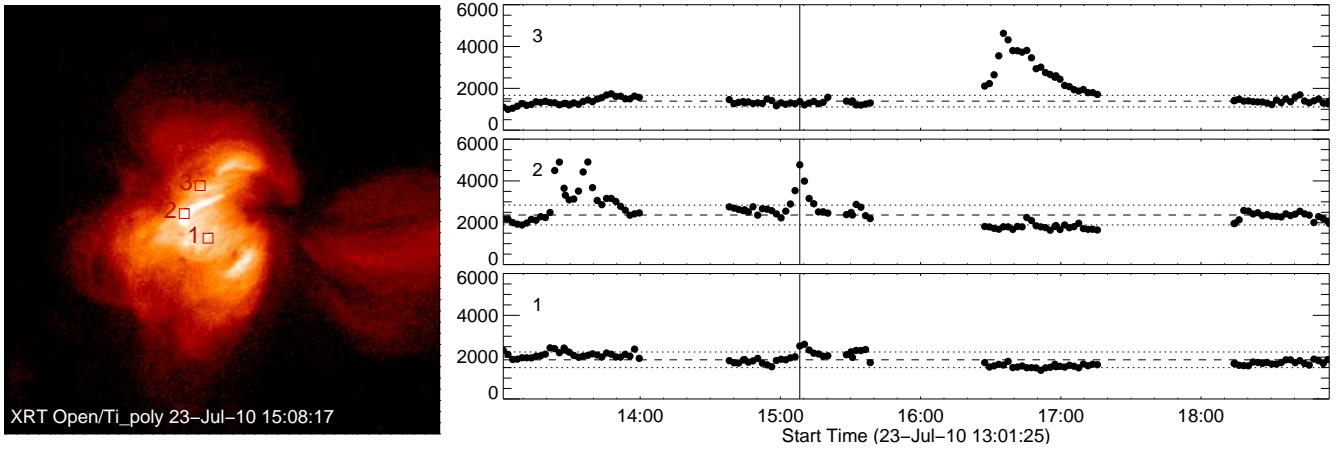


Fig. 3.— XRT observations of AR 11089. On the left is a frame from the observing sequence. On the right are light curves from three different locations in the core of the active region. Intensities are in  $\text{DN s}^{-1}$  per pixel. The dashed horizontal line is the median intensity for the period shown. The dotted horizontal lines are  $\pm 20\%$  of the median. The solid vertical line corresponds to the time of the image. The emission in the core of the active region is relatively constant, with a variability of 20% or less. Transient events with relatively short lifetimes ( $\lesssim 900$  s) are also observed. The electronic version of the manuscript includes a movie of these data.

## 2. Observations and Analysis

In this paper we consider EIS, XRT, and AIA observations of NOAA active region 11089 taken on 2010 July 23. This section gives a brief overview of the various instruments, the available data, and the calculation of the differential emission measure distribution.

The AIA on *SDO* consists of 4 independent normal incidence, multi-layer telescopes, each with 2 channels. Each channel images the full Sun. The AIA coronal channels and their dominant components are as follows: 94 Å (Fe X and Fe XVIII), 131 Å (Fe VIII and Fe XX, Fe XXI, and Fe XXIII), 171 Å (Fe IX and Fe X), 193 Å (Fe XII), 211 Å (Fe XIV), 335 Å (Fe XVI). A detailed discussion of the predicted contributions to each AIA channel is presented by O’Dwyer et al. (2010). The relatively cool components of the 94 and 131 Å channels have been identified in high spectral resolution stellar observations (e.g., Raassen et al. 2002; Liang & Zhao 2010). There is also a He II 304 Å channel and a UV channel. Figure 1 shows sample AIA images from this active region taken near 15 UT. For this work we use the level 1.5 cutout data that has been re-scaled and co-aligned to a common coordinate system. We note that to precisely co-align the data in the various channels we cross-correlated a subset of 20 full-disk images taken from the period of interest. These offsets were generally on the order of 1–2 pixels in each direction. De-rotation of the data was achieved by using established solar rotation rates. As is evident in the movies, there is very little jitter in the data.

The XRT on *Hinode* (Golub et al. 2007) is a grazing incidence, soft X-ray telescope. Temperature discrimination is achieved through the use of focal plane filters. Because XRT can observe the Sun at short wavelengths, XRT can observe high temperature solar plasma very efficiently. For the observations considered here, XRT took images in the thin Ti-poly filter at a cadence of about 120 s, with Al-thick context images taken approximately every 90 minutes. The observing was periodically interrupted by seasonal eclipses that occur annually during the May – August period. Representative XRT Ti-poly and Al-thick images are shown in Figure 1. The XRT images have been co-aligned with respect to the first image in the sequence. The XRT and AIA data were co-aligned by cross-correlating the Ti-poly and 335 Å images. This analysis incorporates the latest available calibration for XRT (Narukage et al. 2010).

The EIS instrument on *Hinode* (Culhane et al. 2007; Korendyke et al. 2006) is a high spatial and spectral resolution imaging spectrograph. EIS observes two wavelength ranges, 171–212 Å and 245–291 Å, with a spectral resolution of about 22 mÅ and a spatial resolution of about 1'' per pixel. Solar images can be made by stepping the slit over a region of the Sun. Telemetry constraints generally limit the spatial and spectral coverage of an observation. For the observations considered here the 1'' slit was stepped over the core of the active region using 60 2'' steps and 512'' of the slit height was read out. The field of view for the EIS raster that was run between 14:32 and 15:34 UT on 2010 July 23 is indicated in Figure 1.

The use of wide 2'' steps in the EIS raster degrades the spatial resolution somewhat, but allows for the raster to be completed in between *Hinode* eclipses even while using relatively long (60 s) exposure time. The use of wide steps also reduces telemetry usage and allows for a very extensive line list to be telemetered to the ground. From these data we have determined intensities for 39 spectral lines. Images for some of these emission lines are shown in Figure 2. Almost all of the line intensities can be determined by simple Gaussian fits. The Ca XVII 192.858 Å line is complicated by blending with Fe XI 192.813 Å and a complex of O V lines, including O V 192.906 Å. The intensities for these lines are determined using the method outlined by Ko et al. (2009), where the intensity of the Fe XI 192.813 Å line is inferred from Fe XI 188.219 Å and the remaining part of the profile is fit with multiple Gaussians. The resulting Ca XVII raster is consistent with Fe XVII 254.87 Å, indicating that the deconvolution is approximately correct.

Collectively, these data suggest a relatively simple morphology to the active region. The EIS emission lines formed at high temperatures, Fe XVI (2.82 MK), Ca XIV (3.55 MK), Ca XV (4.47 MK), Ca XVI (5.01 MK), and Ca XVII (5.62 MK), and the XRT Ti-poly and Al-thick images show relatively short, hot loops that connect across the neutral line running through the middle of the active region. The temperatures given here correspond to the peaks in the CHIANTI 6.0 ionization fractions (Dere et al. 2009). Below these hot loops are regions of intense “moss,” the footpoints of the hot loops that are evident in emission lines formed at temperatures near 1 MK (e.g., Peres et al. 1994; Berger et al. 1999; Fletcher & de Pontieu 1999; Martens et al. 2000). As mentioned earlier, the relatively cool fan-like loops (e.g., Schrijver et al. 1999) appear to be largely absent from the core of the active region. The emission at these temperatures, however, is not



zero. There is certainly diffuse million degree coronal emission lying above the active region. The AIA movies also indicate that there is some million degree emission associated with the very cool, and highly dynamic filament-like material in the core of the active region that connects across the neutral line at very low heights.

As mentioned previously, the primary strength of the XRT is the ability to observe high temperature emission over a wide field of view at relatively high cadence. This is illustrated in Figure 3, where light curves from several positions in the core of the active region are shown. Each light curve is from a single pixel, there is no spatial averaging. Consistent with earlier analysis (e.g., Warren et al. 2010), these light curves show relatively constant emission. Typical intensities generally lie within a range of  $\pm 20\%$  over many hours. Transient brightenings are observed, but they are relatively short lived, with lifetimes of 900 s or less.

The AIA movies, which are included in the electronic version of this manuscript, show that the moss is consistent with the relatively constant emission observed in XRT. The AIA 131 and 171 Å movies show clear evidence for many fine coronal loops in the active region. Few of these loops, however, connect to elements of the moss. There is evidence for intensity fluctuations in the moss itself, but it is likely that this is related to spicular activity that obscures the moss (de Pontieu et al. 1999).

The primary objective of this study is to determine the distribution of temperatures in the hot loops in the core of the active region. We are particularly interested in the conditions at the loop apexes along the line of sight that avoids contamination from the moss emission. Such measurements are important for determining the physical conditions in the high temperature loops. To accomplish this we have determined spatially averaged EIS line profiles in the small “inter-moss” region indicated in Figures 1 and 2. The size of this region is  $10'' \times 15''$  or 75 spatial pixels when we account for the  $2''$  steps. This region has relatively little contamination from the moss or from overlying loops. The spatial averaging diminishes the uncertainties for the intensities of some of the weaker lines and allows for a more complete analysis. The intensities for these line profiles are computed using the same assumptions as the spatially resolved intensities shown in the rasters. The intensities from this region are given in Table 1. The selection of lines is motivated by previous emission measure calculations in the quiet Sun (Brooks et al. 2009; Warren & Brooks 2009) and in flares (Del Zanna 2008; Warren et al. 2008). This previous work has identified emission lines that are mutually consistent. Note that Fe XVII 254.87 Å has been left out because of uncertainties in the atomic data (Warren et al. 2008).

To compute the differential emission measure we use the Monte Carlo Markov Chain (MCMC) emission measure algorithm (Kashyap & Drake 1998, 2000) distributed with the PINTofALE spectral analysis package. This algorithm has the advantage of not assuming a functional form for the differential emission measure. The MCMC algorithm also provides for estimates of the error in the DEM by calculating the emission measure using perturbed values for the intensities. The algorithm assumes the uncertainties in the intensities are uncorrelated so that systematic errors in

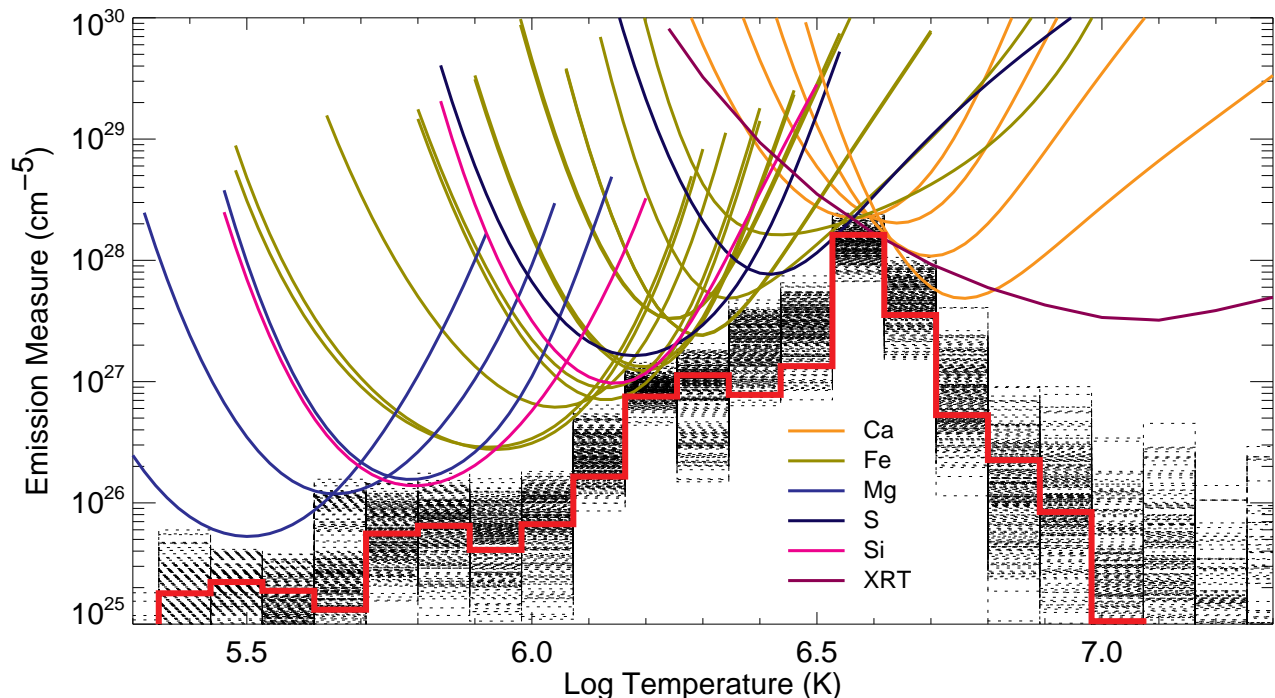


Fig. 4.— The emission measure distribution for the core of the active region. The DEM was computed using the “inter-moss” intensities from EIS and XRT and represents the physical conditions at the loop-tops along the line of sight. The solid red line is the best-fit DEM and the dotted black lines are from Monte Carlo calculations using perturbed values of the observed intensities. 250 Monte Carlo simulations of the emission measure were performed. This gives a statistically plausible range for the emission measure in each temperature bin. The solid lines are the emission measure loci curves described in the text and color-coded according to element. The emission measure distribution is strongly peaked at  $\log T = 6.6$  and falls off sharply for both higher and lower temperatures.

the calibration, which could depend on the wavelength, or in the atomic data, which could vary by ion, are not accounted for.

In its current implementation the MCMC algorithm does not allow for the density to be a free parameter. In principal the Ca XV 181.900/200.972 Å ratio should provide information on the density at temperatures near 4 MK. The weaker component of this line pair, 181.900 Å, however, is not observed in these data. At the densities we expect ( $< 10^{10} \text{ cm}^{-3}$ ) the intensity of the 181.900 Å line is less than 0.1 times that of the 200.972 Å. This implies less than 20 DN would be detected in this 60s observation. Monte Carlo simulations indicate that approximately 100 counts are needed to compute a line intensity. In the absence of alternatives we use the Fe XIII 202.836/202.044 Å ratio, which yields a density of  $\log n_e = 9.45$ . We will discuss this result later in the paper.



The relationship between the emissivities, the differential emission measure, and the observed intensities is the usual expression

$$I_\lambda = \frac{1}{4\pi} \int \epsilon_\lambda(n_e, T_e) \xi(T_e) dT_e, \quad (1)$$

where  $\epsilon_\lambda(n_e, T_e)$  is the emissivity computed with the CHIANTI 6.0.1 atomic database assuming coronal abundances (Feldman et al. 1992) and the new CHIANTI ionization fractions (Dere et al. 2009). The function  $\xi(T_e) = n_e^2 ds/dT_e$  is the differential emission measure distribution inferred from the intensities. Here we also show the emission measure loci computed from

$$\xi_{loci}(T_e) = \frac{4\pi I_\lambda}{\epsilon_\lambda(n_e, T_e)}, \quad (2)$$

which indicates the temperature range where the various lines are sensitive. Note that to aid in the comparisons with the em loci we will always plot the DEM multiplied by the temperature bin,

$$\xi(T_e) dT_e, \quad (3)$$

and we refer to this as the emission measure distribution.

The DEM computed from the MCMC method is shown in Figure 4. The intensities computed from the DEM, which are also given in Table 1, are generally consistent with the observations to within 25%, although there are some significant discrepancies. We note that the Mg lines, which lie at the low end of the temperature range, are not fully consistent with Si VII. We conjecture that this is due to uncertainties in the abundances. Since the intensity for Si X is consistent with the other Fe lines formed at a similar temperature, we assume that this discrepancy is due to the Mg abundance. To compute the emission measure we multiply the coronal Mg abundance by a factor of 1.7 to bring Mg VII 280.737 Å into agreement with Si VII 275.368 Å. In this analysis we have also included two lines from S, which is a low first ionization potential element. The consistency between the S and Fe lines in this DEM calculation suggests that the assumption of coronal abundances is generally valid, at least in a relative sense. Among the Fe lines the most significant problem is for Fe XIII. This is perplexing since there are no such problems evident in the analysis of quiet Sun data. This issue is unresolved here, but the emission measure is meant to be only a crude representation of the temperature distribution in these core active region loops. We will consider comparisons between some simple heating models and the observed intensities in the next section.

The most significant result from this calculation is the fact that the emission measure is strongly peaked at about  $\log T_e = 6.6$  (4 MK) and falls off sharply at both higher and lower temperatures. The peak emission measure is approximately  $10^{28} \text{ cm}^{-5}$  while the emission measure at  $\log T_e = 5.8$ , the temperature of formation for Si VII, is about a factor of 400 less. Because of the broad nature of the Ca XVII and XRT Al-thick responses, the decline in the emission measure at higher temperatures is less certain. The Monte Carlo simulations suggest a fairly broad range of possible emission measures at the higher temperatures, but the vast majority of them lie at the lower end of the range.

Numerous active region emission measure distributions have been published in the literature (e.g., Dere 1982; Dere & Mason 1993; Brosius et al. 1996; Warren et al. 2001; Winebarger et al. 2011; Tripathi et al. 2011). Our emission measure distribution has significantly steeper slopes away from the maximum than most previous results. We attribute this to the fact that most previous work has used intensities derived from averages over large field of view. Our work, in contrast, has focused on a very small region that represents the conditions near the loop apex. Tripathi et al. (2011) and Winebarger et al. (2011) have also considered a small “inter-moss” region and find both shallow and steep slopes from the peak emission measure to lower temperatures. It is clear that a systematic study is required to understand the range of possible emission measure distributions near the loop apex.

In computing the intensities in the active region core or inter-moss region we have not performed any background subtraction. The intensities of the high temperature lines outside of the core are negligible. For the cooler emission lines it is not clear which region to take as the background. The intensities for these lines in the dimmest areas of the active region are typically 10% of the core intensity and close to the core the intensities are comparable. This suggests a very large range of possibilities. In all cases the background subtracted intensities would be lower than the values that we have used. This would lead to even steeper declines in the emission measure distributions at low temperatures. At low temperatures, the emission measure shown in Figure 4 is an upper bound.

### 3. Modeling

Early work on the modeling of high temperature loops observed at soft X-ray wavelengths often focused on steady heating models (e.g., Kano & Tsuneta 1995; Porter & Klimchuk 1995). Such analysis has also yielded volumetric filling factors that were generally less than 1 (Porter & Klimchuk 1995), indicating that the observed loops were unresolved. Such observations could not exclude the possibility that the observed emission only appeared steady, but was actually made up of many unresolved loops that are evolving. The broad temperature coverage of the combined EIS and XRT observations allows us to make much more detailed comparisons with the predictions of different heating scenarios.

In this section we will make quantitative comparisons between the observations and solutions to the hydrodynamic loop equations, which describe the evolution of mass, momentum, and energy in a flux tube. We will consider low-frequency heating, where the time between heating events is long relative to the cooling time, and high-frequency heating, where the loop is reheated before it has time to cool. The goal is to consider some very simple cases that will lay the foundation for more complete studies in the future. The full modeling of all the observed emission in the active region (e.g., Schrijver et al. 2004; Warren & Winebarger 2007; Winebarger et al. 2008; Lundquist et al. 2008; Winebarger et al. 2011) is beyond the scope of this work.

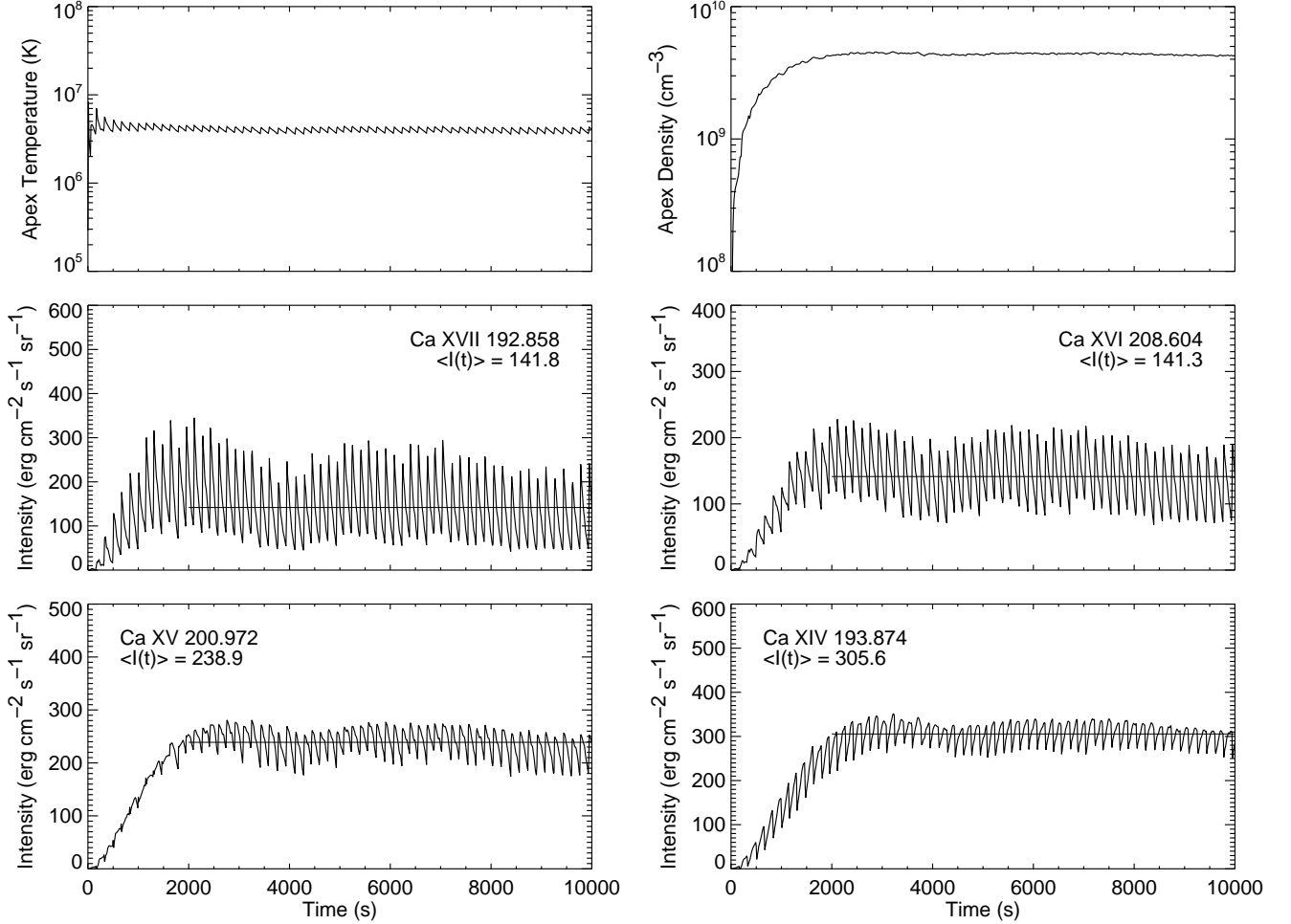


Fig. 5.— An example of high-frequency heating that keeps a loop close to equilibrium. Shown here are the apex temperature and density (*top panels*) in the loop and the apex intensities for four high temperature emission lines (*bottom panels*). For the line emission the average intensity is also indicated. The initial atmosphere for this simulation is very tenuous (0.4 MK initial apex temperature) and the density converges to the asymptotic value slowly so the averaging is done over the final 8,000 s of the simulation.

The loop length is an important parameter in any hydrodynamic simulation. The AIA images suggest a distance of approximately 50 Mm between the middle of the moss regions in this active region. This implies a total loop length ( $L$ ) of approximately 75 Mm for a semi-circular loop that is perpendicular to the solar surface. For simplicity we will consider a single loop length in the simulations. A radiative loss rate as a function of temperature must also be specified. The DEM calculation presented in the previous section showed that the observed intensities for S X and S XIII are consistent with coronal abundances so we will assume a radiative loss curve computed using

the coronal abundances of Feldman et al. (1992).

To solve the time-dependent hydrodynamic loop equations we use the NRL Solar Flux Tube Model (SOLFTM). We adopt many of the same parameters and assumptions that were used in previous simulations with this code and we refer the reader to the earlier papers for additional details on the numerical model (e.g., Mariska et al. 1989; Warren et al. 2003). To establish a characteristic time scale for the cooling of a high temperature loop with a total length of 75 Mm and a coronal composition, we begin by considering an initial simulation of a loop in equilibrium with an apex temperature of 4 MK, the peak temperature in the DEM. If the loop is allowed to cool without any additional heating the apex temperature reaches 0.5 MK in approximately 1200 s, we will use  $\tau_c$  to represent this cooling time.

To model emission that persists we need to specify the volumetric heating rate as a function of time. We consider a series of step-function heating events that have a magnitude  $\epsilon$ , a duration  $\delta$ , and an occurrence rate  $\tau$ . We will assume that  $\delta < \tau$  for these simulations. We will also assume that the heating is uniform over the loop length. The mean heating rate is simply

$$\bar{\epsilon} = \frac{\epsilon \cdot \delta}{\tau}. \quad (4)$$

For a given loop length and radiative loss curve the parameter  $\bar{\epsilon}$  determines, at least approximately, the average apex temperature for the loop. For this work we will assume  $\bar{\epsilon} = 8.31 \times 10^{-3} \text{ erg cm}^{-3} \text{ s}^{-1}$ , which is the heating rate required to keep the loop in equilibrium with an apex temperature of approximately 4 MK, and we will vary  $\epsilon$ ,  $\delta$ , and  $\tau$  subject to this constraint.

An estimate of the event occurrence rate was given by Cargill (1994) using

$$\tau \sim \frac{Q}{\Lambda A_h}, \quad (5)$$

where  $Q$  is the average event energy,  $\Lambda$  is the radiative loss rate of the corona, and  $A_h$  is the spatial scale for coronal loops. For  $Q \sim 10^{24} \text{ erg}$ ,  $A_h \sim 10^{14} \text{ cm}^2$ , and  $\Lambda \sim 10^7 \text{ erg cm}^{-2} \text{ s}^{-1}$  the time scale is  $\tau \sim 1000 \text{ s}$ . Since these parameters are simply estimates there is a considerable range of possible values for  $\tau$ . With the application of the appropriate geometrical factors Equation 4 can be recast in a form similar to Equation 5. Our preference is to use the volumetric heating rate since it is the input to the hydrodynamic loop equations.

For high-frequency heating ( $\tau \ll \tau_c$ ) we expect the loop to be close to equilibrium. To illustrate an example of such a loop we consider the parameters  $\tau = 150 \text{ s}$ ,  $\delta = 13 \text{ s}$ , and  $\epsilon = 9.28 \times 10^{-2} \text{ erg cm}^{-3} \text{ s}^{-1}$ . To simplify the discussion we average the solution over the top 50% of the loop length at each time step to determine the apex density and temperature as a function of time. We then compute the time-dependent intensity of each emission line of interest using

$$I_\lambda = \frac{1}{4\pi} \epsilon_\lambda(n_e, T_e) n_e^2 ds. \quad (6)$$

We infer the path length ( $ds$ ) from the observed Ca XV 200.972 Å intensity and use this value in calculating the intensities for all of the other lines. For this example the path length is 12.3 Mm.

Finally, to approximate the superposition of many sub-resolution strands in various stages of heating and cooling we compute the time-averaged intensity (e.g., Patsourakos & Klimchuk 2006; Warren & Winebarger 2007). The resulting apex temperatures and densities, are shown in Figure 5 along with the intensities for the high temperature Ca lines. All of the simulated and observed intensities are given in Table 2.

For this set of parameters the high temperature emission lines (above  $\log T = 6.45$ ) are generally well produced by the model. Since heating events occur very frequently the temperatures and densities in the loop are never too far from their average values ( $\log T = 6.60$  and  $\log n_e = 9.64$ ), and the loop never cools. These simulation results are from a family of simulations where the heating duration  $\delta$  and heating rate  $\epsilon$  were varied. For larger values of delta the departures from the average temperature is smaller and the intensity in Ca XVII becomes much smaller than what is observed. Similarly, for smaller values of delta the intensities in Ca XVII are larger and also inconsistent with what is observed.

The intensities for the lower temperature emission are not reproduced by this model. Since the loop never cools, the modeled intensities at low temperatures are close to zero. One possible interpretation is that the relatively weak cool emission is unrelated to the high temperature active region loops and comes from either very low-lying loops or very long loops that extend over the active region.

For  $\tau \gtrsim \tau_c$  the loop will evolve over a large range of temperatures and will be far from equilibrium. To illustrate an example of the low-frequency heating that is usually assumed in nano-flare modeling we consider the parameters  $\tau = 1800$  s,  $\delta = 67$  s, and  $\epsilon = 2.22 \times 10^{-1}$  erg cm $^{-1}$  s $^{-1}$ . The apex temperatures and densities from this simulation are shown in Figure 6. These parameters give approximately the same mean temperature and density ( $\log T = 6.54$  and  $\log n_e = 9.62$ ) as in the previous case. In addition to the high temperature Ca lines we also show the evolution of Fe XII 195.119 Å and Si VII 275.368 Å in Figure 6. The path length inferred from the Ca XV intensity is 25.2 Mm. All of the simulated and observed intensities are given in Table 2.

In this case the long time between heating events allows the loop to cool and there is significant emission for lines formed at low temperatures. These intensities, however, are much larger than what is observed. For Si VII 275.368 Å, for example, the modeled intensity is almost a factor of 10 times too large. The difficulty for the low-frequency heating scenario is the slow draining of the density from the loop. Previous work has suggested an  $n_e \sim \sqrt{T_e}$  relationship (Jakimiec et al. 1992; see also the more recent work by Bradshaw & Cargill 2010 which refines this scaling law). This leads to relatively large densities and thus large intensities at low temperatures.

The low-frequency heating case also has difficulties with the high temperature emission. The modeled intensities for Ca XVII 192.858 Å and XRT Al-thick are larger than what is observed. This simulation is from a family of simulations with different values for  $\delta$  and  $\epsilon$ . For the cases we considered ( $\delta < 100$  s) the intensities for this emission was always about a factor of 3 greater than what is observed. This seems to be an inevitable consequence of low frequency heating. To produce

relatively high densities with short bursts of heating the magnitude must be large, which leads to high temperatures and large Ca XVII 192.858 Å and XRT Al-thick intensities.

As mentioned previously, the power law index that we measure in the emission measure distribution between the peak near  $\log T = 6.6$  and lower temperatures is steeper than most previous measurements and steeper than is expected from simple heating models, which can have a emission measure that scales like  $\sim T^{3/2}$  (e.g., Jordan 1976). This is likely a result of averaging over a small region near the loop apexes in the observations. To demonstrate this we have calculated the emission measure distributions, essentially histograms of  $n_e^2 ds$ , from both the high- and low-frequency heating simulations. These distributions, which are shown in Figure 7, clearly illustrate the effect of averaging. The power-law index ( $b$  in  $EM \sim T^b$ ) for the entire loop is smaller ( $b \lesssim 1.5$ ) than for the loop apex ( $b \gtrsim 2$ ).

One objection that could be raised regarding the emission measure distribution is that the box used to compute the average intensities is small and these values are not representative. The contrast between the moss and inter-moss regions at low temperatures, however, is small. For Si VII 275.368 Å, for example, the intensities only increase by a factor of about 2 in the moss. It is clear that the large discrepancy between the intensities computed from the low-frequency heating scenario would not be changed significantly by modifying the region used for the averaging.

Since the rasters for the lowest temperature lines are relatively noisy, it is tempting to think that these lines are simply too faint to measure reliably. As we illustrate in Figure 8, however, the emissivity for Si VII 275.368 Å, which is one of the primary EIS lines at low temperatures is actually higher than the emissivity for the high temperature Fe XVI 262.984 Å line, which is easily observed in the core of the active region. The effective area for EIS at these wavelengths is also very similar. Absent some fundamental flaw in the hydrodynamic models, it appears that any hot plasma evident in the Fe XVI 262.984 Å line would be easily observed in Si VII 275.368 Å as it cooled.

The emissivities for the hot lines shown in Figure 8 suggest similar inconsistencies between the observations and low-frequency, impulsive heating scenarios. The emissivity for Ca XVII 192.858 Å is higher than that for Ca XIV 193.874 Å, suggesting that loops that have been heated up to very high temperatures ( $\sim 10$  MK) and are cooling would show comparable intensities in these lines. Instead, the data show that the Ca XVII emission is weaker than the emission from Ca XIV. Again, the observations are difficult to reconcile with traditional hydrodynamic models of impulsively heated loops.

#### 4. AIA

As we have already seen in Figure 1, AIA’s combination of high cadence, high spatial resolution, and broad temperature coverage provide new ways to explore the temperature structure of an active region. Of particular interest to studies of high temperature active region loops is the 94 Å channel,



which contains the Fe XVIII 93.94 Å formed at about 7 MK. Also of interest is the 131 Å channel, which contains Fe XX, Fe XXI, and Fe XXII lines. Another channel not previously flown is the 335 Å channel, which images Fe XVI 335.4 Å. In Figure 8 we show the isothermal temperature response curves for the AIA 171, 335, 94, and 131 Å channels along with the emissivities for the EIS high temperature lines (Fe XVI and Ca XIV–Ca XVII), and the two XRT channels considered in this paper.

The AIA 94 Å channel is of particular interest because it combines high spatial and temporal resolution with a relatively narrow temperature response. The EIS emission lines are formed at somewhat lower temperatures and, at least for these observations, have no temporal resolution. XRT observes these temperatures at high cadence, but has a very broad temperature response. Since the cross-calibration of the AIA instrument is just beginning at this point, we’re interested only in some very basic questions, such as what is the morphology of the emission in this channel and how does it evolve with time?

To provide some context for interpreting the AIA 94 Å and 131 Å channels we have used the simulations results for the high and low frequency heating cases shown in Figures 5 and 6 to compute the expected count rates in these channels. As one would expect, we find that the amount of high temperature emission observed in these channels is sensitive to the heating time scale. For the low-frequency heating case, which reaches temperatures close to 10 MK, observable emission ( $\sim 50\text{--}100 \text{ DN s}^{-1}$ ) is predicted for both channels. The high-frequency case shows some signal in the 94 Å channel but relatively little in 131 Å. These comparisons suggest that these channels will provide important information on the heating time scale. Quantitative comparisons, however, will require the AIA calibration to be more fully understood. Also, at these high temperatures the potential for departures from ionization equilibrium are much greater.

It is clear from the movie of the 94 Å channel, which is available in the electronic version of the manuscript, that there is significant emission from Fe XVIII in the core of the active region. This channel, however, also contains contributions from lines formed at lower temperatures. Comparisons with the 171 Å channel allow us to identify the high temperature, Fe XVIII loops. Such comparisons suggest that the bulk of the Fe XVIII emission lies at the inner edge of the moss on loops that connect directly across the neutral line.

To address the question of temporal evolution we have taken the co-aligned and de-rotated data cubes used to make the movies and computed light curves for various points in the active region. Light curves for three points are shown in Figure 9. One of the points illustrates the evolution of a small flare. Here the light curves show the progression from the high temperature flare emission of Fe XX–Fe XXIII, to the hot Fe XVIII and Fe XVI, to the relatively cool Fe IX. This qualitative agreement between the observations and our expectations for a flare light curve suggests that the emission lines contributing to each channel are properly identified. Other small “microflaring” events show a similar progression, except that the cooling to the lowest temperatures is difficult to identify (middle panel). Finally, the majority of the pixels in the core of the active region do not

show coherent behavior. In these pixels the intensities measured in the 131 and 171 Å channels are well correlated, suggesting an absence of plasma at flare temperatures. For these points the 94 and 335 Å channels do not show any obvious correlation. There is no general tendency for brightenings in the 94 Å channel to be followed by brightenings in 335 Å. This is potentially consistent with the high-frequency heating scenario, but will require more quantitative analysis to demonstrate conclusively.

## 5. Discussion

We have presented the detailed analysis of high temperature active region core loops using observations from *Hinode* and *SDO*. The primary result is the calculation of the emission measure, which shows a sharp peak at about 4 MK and a steep decline at both higher and lower temperatures. These observations provide a difficult challenge to the low-frequency heating scenarios that have traditionally been associated with nanoflare heating models of the corona. As we’ve shown with some very simple hydrodynamic simulations, such models predict significant emission at lower temperatures, but the observed emission measure below 1 MK is generally small in the core of an active region near the loop apexes. A high-frequency heating scenario, in contrast, agrees with the observed intensities of the high temperature emission lines, is consistent with the relatively steady emission observed in XRT, and with the absence of cooling loops in the moss in the cool AIA channels (e.g., 171 Å).

Our analysis provides compelling evidence that there is a significant population of loops in the core of a solar active region that are heated on very short time scales, much shorter than a typical cooling time for this combination of density ( $\log n_e \sim 9.7$ ), temperature ( $\log T_e \sim 6.6$ ), and loop length ( $L \sim 75$  Mm). We suggest that this combination of parameters is a useful set for theorists to consider in developing physical models of high temperature coronal loops. The challenge is to identify a physical mechanism that not only reproduces these conditions, but is also frequent enough to keep the loop at high temperatures for long periods of time.

One limitation of the high-frequency heating scenario, however, is that it does not reproduce the emission that is observed at low temperatures. In the emission measure distributions shown in Figure 7, for example, it is clear that the result from the high-frequency simulation is close to observed distribution at high temperatures (above  $\log T = 6.5$ ), but significantly under-predicts the distribution at low temperatures. One possibility is that there is a range of heating time scales at work in the solar atmosphere. Brooks et al. (2008) and Lee et al. (2010), for example, have suggested a relationship between magnetic topology and the variability of the heating. Transient brightenings appear to be associated with magnetic complexity, while magnetically simple regions show relatively constant emission. Motivated by the emission measure distributions shown in Figure 4 we have constructed composite intensities with 90% high-frequency heating and 10% low-frequency heating. As is shown in Table 2, this simple mixture provides a better match to the observations at both high and low temperatures. This doesn’t provide a consistent description for

all of the lines, but does suggest how a complete description of the observed emission might be achieved.

We stress that the hydrodynamic simulations presented here represent a very small set of possible heating scenarios. Some 0D impulsive heating models have produced relatively steep slopes in the emission measure distribution (e.g., Cargill 1994; Klimchuk et al. 2008). We have had trouble reproducing these results with hydrodynamic simulations and we are currently investigating this systematically. Other considerations, such as variations in loop length along the line of sight, differences in initial conditions, or accounting for non-equilibrium ionization, may bring low-frequency, nanoflare heating models into better agreement with the observations. Much more extensive analysis is required. One significant hurdle that all models must clear is reproducing the observed intensities both in the corona and at the footpoints. The next step in this analysis is to couple hydrodynamic simulations to topology derived from magnetic field extrapolations and attempt to reproduce all of the emission observed in the active region.

Hinode is a Japanese mission developed and launched by ISAS/JAXA, with NAOJ as domestic partner and NASA and STFC (UK) as international partners. It is operated by these agencies in co-operation with ESA and NSC (Norway). The authors would like to thank the referee for many valuable comments on the manuscript.

## REFERENCES

- Antiochos, S. K., Karpen, J. T., DeLuca, E. E., Golub, L., & Hamilton, P. 2003, *ApJ*, 590, 547
- Berger, T. E., de Pontieu, B., Schrijver, C. J., & Title, A. M. 1999, *ApJ*, 519, L97
- Bradshaw, S. J., & Cargill, P. J. 2010, *ApJ*, 717, 163
- Brooks, D. H., Ugarte-Urra, I., & Warren, H. P. 2008, *ApJ*, 689, L77
- Brooks, D. H., & Warren, H. P. 2009, *ApJ*, 703, L10
- Brooks, D. H., Warren, H. P., Williams, D. R., & Watanabe, T. 2009, *ApJ*, 705, 1522
- Brosius, J. W., Davila, J. M., Thomas, R. J., & Monsignori-Fossi, B. C. 1996, *ApJS*, 106, 143
- Cargill, P. J. 1994, *ApJ*, 422, 381
- Culhane, J. L., et al. 2007, *Sol. Phys.*, 243, 19
- de Pontieu, B., Berger, T. E., Schrijver, C. J., & Title, A. M. 1999, *Sol. Phys.*, 190, 419
- Del Zanna, G. 2008, *A&A*, 481, L69
- Dere, K. P. 1982, *Sol. Phys.*, 77, 77

- Dere, K. P., Landi, E., Young, P. R., Del Zanna, G., Landini, M., & Mason, H. E. 2009, *A&A*, 498, 915
- Dere, K. P., & Mason, H. E. 1993, *Sol. Phys.*, 144, 217
- Feldman, U., Mandelbaum, P., Seely, J. F., Doschek, G. A., & Gursky, H. 1992, *ApJS*, 81, 387
- Fletcher, L., & de Pontieu, B. 1999, *ApJ*, 520, L135
- Golub, L., et al. 2007, *Sol. Phys.*, 243, 63
- Jakimiec, J., Sylwester, B., Sylwester, J., Serio, S., Peres, G., & Reale, F. 1992, *A&A*, 253, 269
- Jordan, C. 1976, *Royal Society of London Philosophical Transactions Series A*, 281, 391
- Kano, R., & Tsuneta, S. 1995, *ApJ*, 454, 934
- Kashyap, V., & Drake, J. J. 1998, *ApJ*, 503, 450
- Kashyap, V., & Drake, J. J. 2000, *Bulletin of the Astronomical Society of India*, 28, 475
- Klimchuk, J. A., & Cargill, P. J. 2001, *ApJ*, 553, 440
- Klimchuk, J. A., Patsourakos, S., & Cargill, P. J. 2008, *ApJ*, 682, 1351
- Ko, Y., Doschek, G. A., Warren, H. P., & Young, P. R. 2009, *ApJ*, 697, 1956
- Korendyke, C. M., et al. 2006, *Appl. Opt.*, 45, 8674
- Kosugi, T., et al. 2007, *Sol. Phys.*, 243, 3
- Lee, J., Barnes, G., Leka, K. D., Reeves, K. K., Korreck, K. E., Golub, L., & DeLuca, E. E. 2010, *ApJ*, 723, 1493
- Liang, G. Y., & Zhao, G. 2010, *MNRAS*, 405, 1987
- Lundquist, L. L., Fisher, G. H., Metcalf, T. R., Leka, K. D., & McTiernan, J. M. 2008, *ApJ*, 689, 1388
- Mariska, J. T., Emslie, A. G., & Li, P. 1989, *ApJ*, 341, 1067
- Martens, P. C. H., Kankelborg, C. C., & Berger, T. E. 2000, *ApJ*, 537, 471
- Narukage, N., et al. 2010, *ArXiv e-prints*
- Nitta, N. 2000, *Sol. Phys.*, 195, 123
- O’Dwyer, B., Del Zanna, G., Mason, H. E., Weber, M. A., & Tripathi, D. 2010, *A&A*, 521, A21
- Parker, E. N. 1972, *ApJ*, 174, 499

- Parker, E. N. 1983, *ApJ*, 264, 642
- Patsourakos, S., & Klimchuk, J. A. 2006, *ApJ*, 647, 1452
- Peres, G., Reale, F., & Golub, L. 1994, *ApJ*, 422, 412
- Porter, L. J., & Klimchuk, J. A. 1995, *ApJ*, 454, 499
- Raassen, A. J. J., et al. 2002, *A&A*, 389, 228
- Schrijver, C. J., Sandman, A. W., Aschwanden, M. J., & De Rosa, M. L. 2004, *ApJ*, 615, 512
- Schrijver, C. J., et al. 1999, *Sol. Phys.*, 187, 261
- Tripathi, D., Klimchuk, J. A., & Mason, H. E. 2011, *ApJ*, submitted
- Warren, H. P., & Brooks, D. H. 2009, *ApJ*, 700, 762
- Warren, H. P., Feldman, U., & Brown, C. M. 2008, *ApJ*, 685, 1277
- Warren, H. P., Mariska, J. T., & Lean, J. 2001, *J. Geophys. Res.*, 106, 15745
- Warren, H. P., & Winebarger, A. R. 2007, *ApJ*, 666, 1245
- Warren, H. P., Winebarger, A. R., & Brooks, D. H. 2010, *ApJ*, 711, 228
- Warren, H. P., Winebarger, A. R., & Mariska, J. T. 2003, *ApJ*, 593, 1174
- Winebarger, A. R., Schmelz, J. T., Warren, H. P., Saar, S. H., & Kashyap, V. L. 2011, *ApJ*, submitted
- Winebarger, A. R., Warren, H. P., & Falconer, D. A. 2008, *ApJ*, 676, 672

Table 1. Differential Emission Measure Model<sup>a</sup>

Line	$T_{max}$	$I_{obs}$	$\sigma_I$	$I_{dem}$	$R$
Mg V 276.579	5.45	16.5	3.8	19.5	0.85
Mg VI 270.394	5.65	35.9	7.9	27.6	1.30
Mg VII 280.737	5.80	32.7	7.4	29.7	1.10
Si VII 275.368	5.80	47.0	10.4	54.3	0.87
Fe IX 197.862	5.85	40.0	8.8	39.7	1.01
Fe IX 188.497	5.85	72.4	16.0	67.0	1.08
Fe X 184.536	6.05	280.4	61.8	202.0	1.39
Si X 258.375	6.15	294.0	64.7	321.2	0.92
Fe XI 188.216	6.15	578.2	127.2	556.0	1.04
Fe XI 180.401	6.15	926.1	204.2	1120.2	0.83
S X 264.233	6.15	71.8	15.9	73.9	0.97
Fe XII 195.119	6.20	1475.4	324.6	1491.6	0.99
Fe XII 192.394	6.20	437.8	96.3	478.5	0.91
Fe XIII 202.044	6.25	1248.3	274.7	665.9	1.87
Fe XIII 203.826	6.25	2533.9	557.6	1331.4	1.90
Fe XIV 270.519	6.30	515.0	113.3	523.0	0.98
Fe XIV 264.787	6.30	1026.9	226.0	1028.8	1.00
Fe XV 284.160	6.35	10334.0	2273.6	11634.3	0.89
S XIII 256.686	6.40	854.7	188.1	853.2	1.00
Fe XVI 262.984	6.45	1157.6	254.7	1138.9	1.02
Ca XIV 193.874	6.55	311.9	68.6	276.3	1.13
Ca XV 200.972	6.65	238.9	52.6	195.7	1.22
Ca XVI 208.604	6.70	122.0	28.3	108.7	1.12
Ca XVII 192.858	6.75	146.5	32.3	128.5	1.14
Open/Al-thick	7.10	4.5	0.9	5.8	0.78

<sup>a</sup>Calculated intensities are from the MCMC emission measure inversion. Intensities are in units of  $\text{erg cm}^{-2} \text{s}^{-1} \text{sr}^{-1}$ .



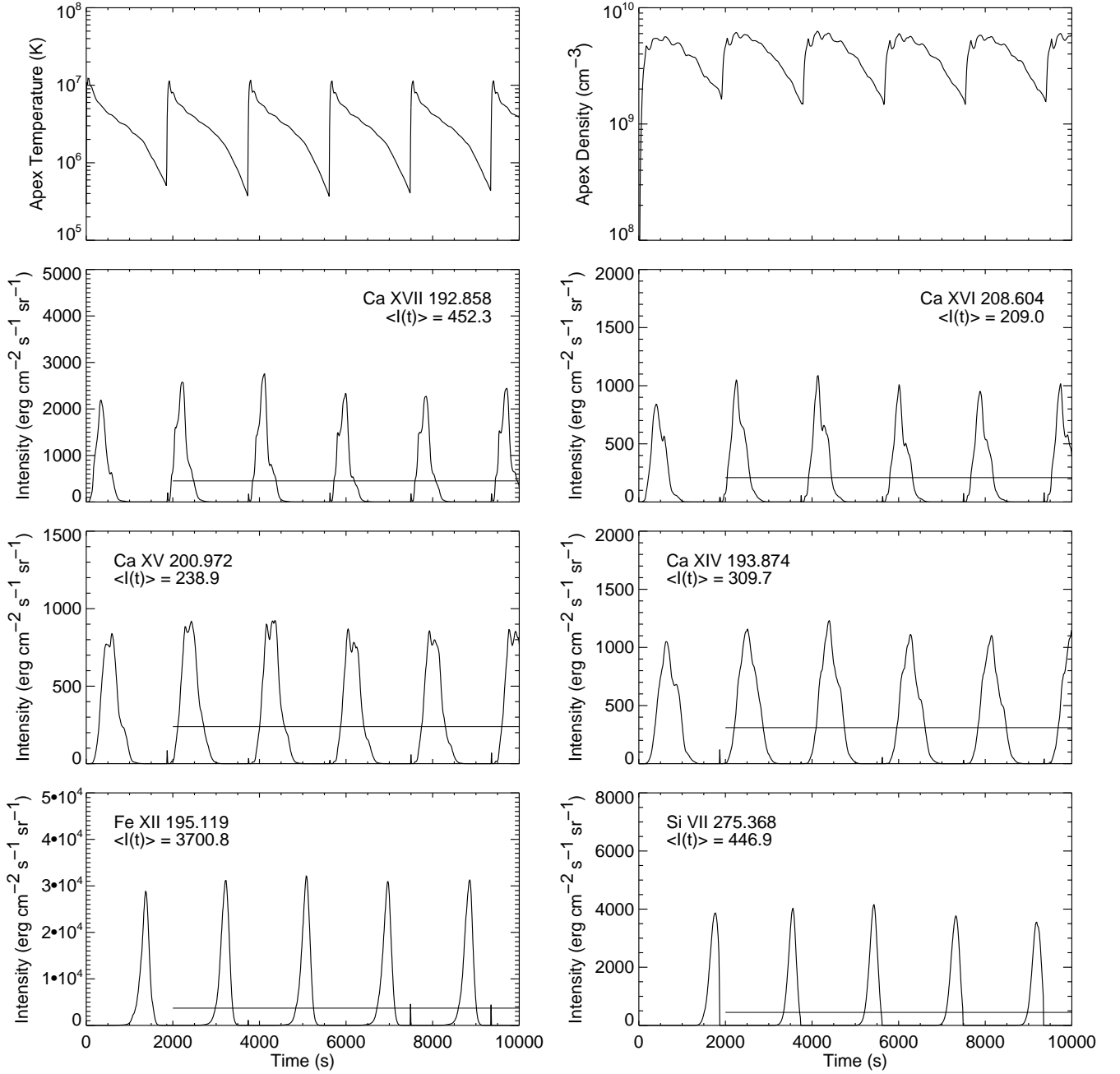


Fig. 6.— An example of low-frequency heating where the long time between heating events allows the loop to evolve over a wide range of temperatures. The top panels show the temperature and density averaged over the loop apex. The bottom panels show the evolution of the intensities in selected emission lines. The time averaged intensities, again taken over the final 8,000 s of the simulation are also indicated. The large intensities calculated for Fe XII 195.119  $\text{\AA}$  and Si VII 275.368  $\text{\AA}$  are not consistent with the observations.

Table 2. Observed and Simulated Active Region Core Intensities<sup>a</sup>

Line	$T_{max}$	$I_{obs}$	$\sigma_I$	$\tau = 150\text{ s}$		$\tau = 1800\text{ s}$		Mixed	
				$I_{model}$	$R$	$I_{model}$	$R$	$I_{model}$	$R$
Mg V 276.579	5.45	16.5	3.8	0.0	>10	57.5	0.3	5.8	2.9
Mg VI 270.394	5.65	35.9	7.9	0.0	>10	200.5	0.2	20.1	1.8
Mg VII 280.737	5.80	32.7	7.4	0.0	>10	213.7	0.2	21.4	1.5
Si VII 275.368	5.80	47.0	10.4	0.0	>10	446.9	0.1	44.7	1.1
Fe IX 197.862	5.85	40.0	8.8	0.0	>10	302.2	0.1	30.2	1.3
Fe IX 188.497	5.85	72.4	16.0	0.0	>10	509.1	0.1	50.9	1.4
Fe X 184.536	6.05	280.4	61.8	0.0	>10	1046.8	0.3	104.7	2.7
Si X 258.375	6.15	294.0	64.7	4.4	>10	958.3	0.3	99.8	2.9
Fe XI 188.216	6.15	578.2	127.2	0.1	>10	1754.6	0.3	175.6	3.3
Fe XI 180.401	6.15	926.1	204.2	0.1	>10	3507.1	0.3	350.8	2.6
S X 264.233	6.15	71.8	15.9	0.6	>10	205.0	0.3	21.0	3.4
Fe XII 195.119	6.20	1475.4	324.6	2.5	>10	3700.8	0.4	372.3	4.0
Fe XII 192.394	6.20	437.8	96.3	0.8	>10	1187.5	0.4	119.5	3.7
Fe XIII 202.044	6.25	1248.3	274.7	10.2	>10	1465.2	0.9	155.7	8.0
Fe XIII 203.826	6.25	2533.9	557.6	23.4	>10	3446.9	0.7	365.8	6.9
Fe XIV 270.519	6.30	515.0	113.3	84.6	6.1	1343.2	0.4	210.5	2.4
Fe XIV 264.787	6.30	1026.9	226.0	177.8	5.8	2829.7	0.4	443.0	2.3
Fe XV 284.160	6.35	10334.0	2273.6	6823.7	1.5	23716.4	0.4	8513.0	1.2
S XIII 256.686	6.40	854.7	188.1	603.4	1.4	1567.7	0.6	699.8	1.2
Fe XVI 262.984	6.45	1157.6	254.7	1078.9	1.1	1741.8	0.7	1145.2	1.0
Ca XIV 193.874	6.55	311.9	68.6	305.6	1.0	309.7	1.0	306.0	1.0
Ca XV 200.972	6.65	238.9	52.6	238.9	1.0	238.9	1.0	238.9	1.0
Ca XVI 208.604	6.70	122.0	28.3	141.3	0.9	209.0	0.6	148.1	0.8
Ca XVII 192.858	6.75	146.5	32.3	141.8	1.0	452.3	0.3	172.9	0.8
XRT Open/Al-thick	7.10	4.5	0.9	6.3	0.7	14.9	0.3	7.2	0.6

<sup>a</sup>All intensities are in units of  $\text{erg cm}^{-2} \text{ s}^{-1} \text{ sr}^{-1}$ . The parameter  $R$  is the ratio of the observed to modeled intensities and  $\tau$  is time between heating events. Mixed refers to a combination of 90% high frequency and 10% low frequency intensities.

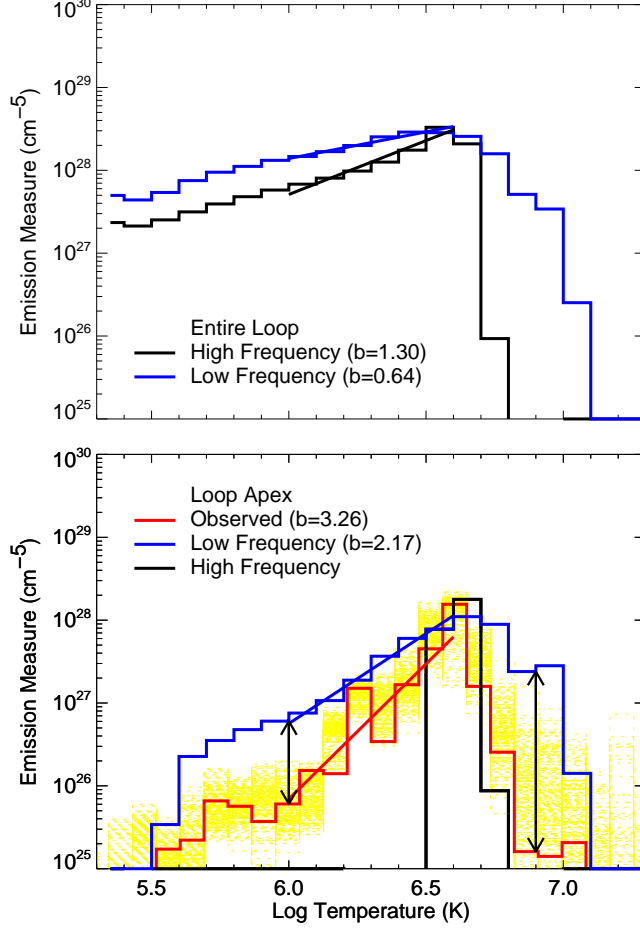


Fig. 7.— The emission measure distributions derived from the high- and low-frequency heating simulations. The distribution for both the entire loop (*top panel*) and loop apex (*bottom panel*) are shown. For comparison, our observed emission measure distribution is also shown in the bottom panel. The arrows indicate the differences between the observation and the low-frequency model at  $\log T = 6.0$  and  $6.9$ . The power law indexes ( $EM \sim T^b$ ) are indicated for several of the emission measure distributions.

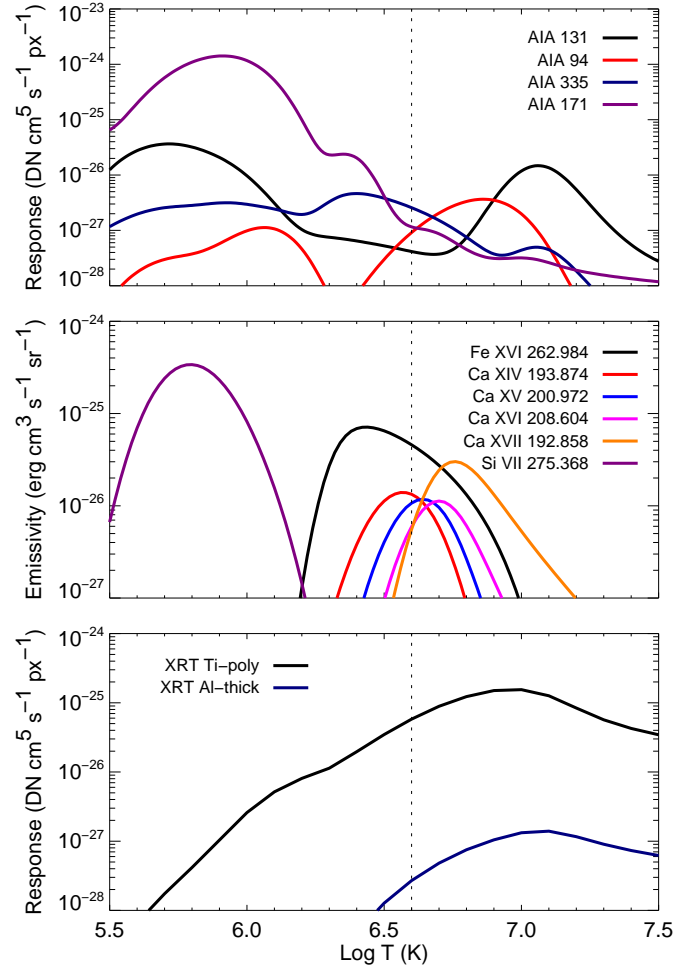


Fig. 8.— Response curves for AIA, EIS, and XRT illustrating the temperature sensitivity of the various images and emission lines. The dotted vertical line indicates the peak temperature in the emission measure distribution.

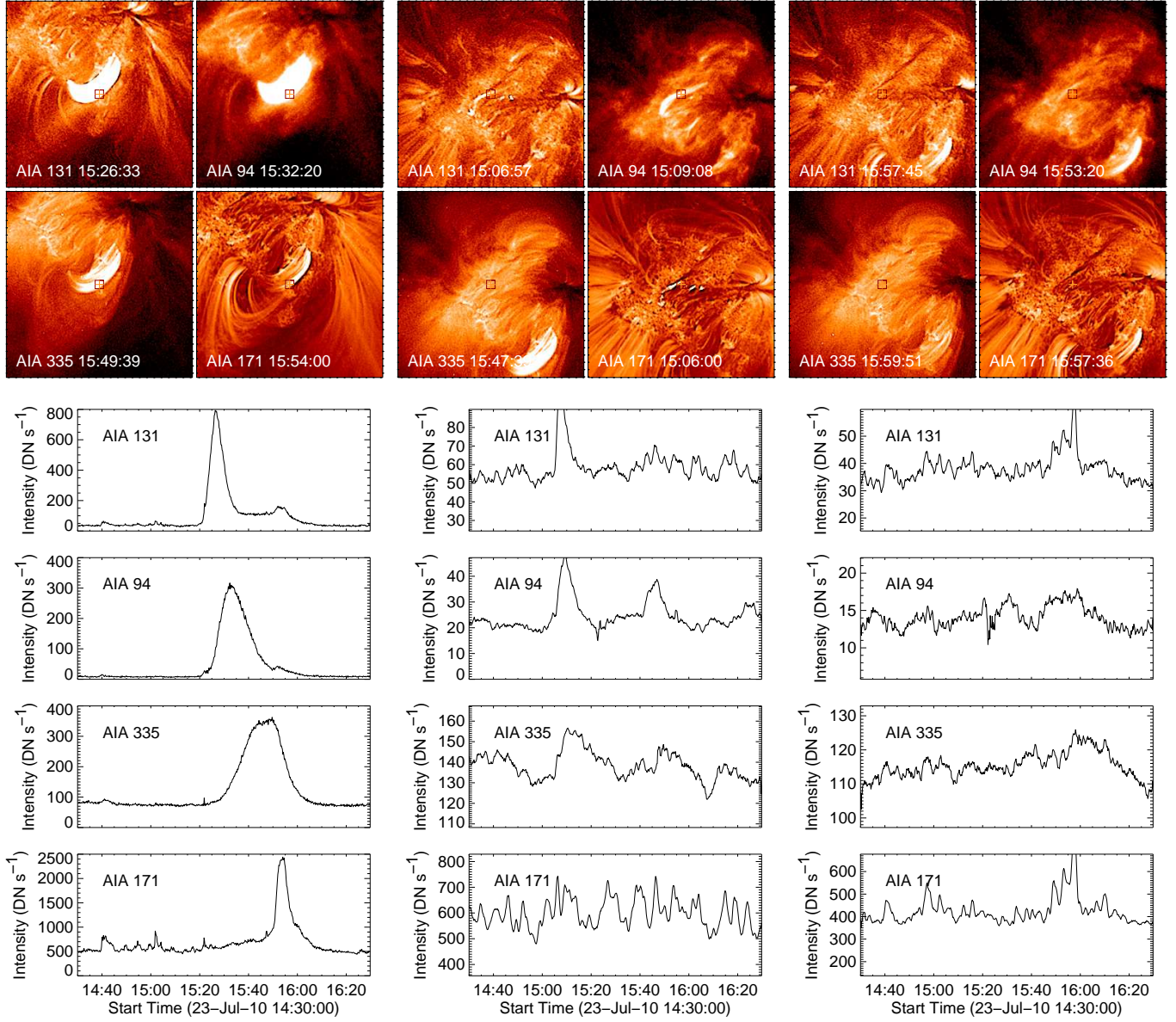


Fig. 9.— Three representative light curves from the core of the active region. The top panels show the image data from the peak of the light curve. The bottom panels show the intensities as a function of time, the intensities have been smoothed with 60 s running averages. The first column shows the evolution of a small flare, with a clear progression from high temperatures (Fe XX–Fe XXIII) to low temperatures (Fe IX). The middle column shows a similar behavior for a microflare. The final column shows the time history of a relatively quiescent pixel in the active region core.